

Contents lists available at ScienceDirect

# Physica A

journal homepage: www.elsevier.com/locate/physa



# Disruption and recovery of reaction—diffusion wavefronts interacting with concave, fractal, and soft obstacles



Yang F. Yu, Chase A. Fuller, Margaret K. McGuire, Rebecca Glaser, Nathaniel J. Smith, Niklas Manz\*, John F. Lindner

Department of Physics, The College of Wooster, Wooster, OH 44691, USA

#### ARTICLE INFO

Article history:
Received 30 May 2020
Received in revised form 8 October 2020
Available online 16 November 2020

Keywords:
Chemical clock
Fractal
Nonlinear wave
Numerical simulation
Obstacle
Reaction-diffusion system

#### ABSTRACT

In a recent publication (Smith et al., 2019), we documented the distinct recovery of reaction–diffusion wavefronts disrupted by hard convex obstacles. Here, we extend that work to include concave, spiral, fractal, random, and soft obstacles. Curvature dependent wavefront velocities ultimately restore the wavefronts, with perturbations that decay as power-law functions of time. But concave, spiral, and fractal obstacles can sustain wavefronts locally for long times. Soft obstacles with variable diffusivity, either intrinsically or due to light sensitivity, can enforce one-way propagation and, appropriately configured, can locally and indefinitely sustain incident wavefronts, creating clocks or repeaters, beating hearts for these excitable systems.

© 2020 Elsevier B.V. All rights reserved.

#### 1. Introduction

Reaction-diffusion wavefronts are fascinating self-organizing phenomena found in many physical, chemical, and biological systems. They characterize, for example, aggregating cell colonies [1], pigmentation lines propagating on the skin of mutant mice [2], oxidation of carbon monoxide on Pt(110) surfaces [3], corroding metals in electrochemical systems [4], and chemical liquid-phase reactions such as the Belousov–Zhabotinsky system [5,6]. Reaction–diffusion waves can also be found within the human body in tissues such as cortical [7], cardiac [8], and gastric [9], or within the uterus [10].

Using computer simulations inspired by the famous Belousov–Zhabotinsky reaction, we have previously documented the disruption and recovery of such wavefronts interacting with hard convex objects [11]. Here we extend that work to include concave, spiral, fractal, random, and soft obstacles. Fig. 1 previews a few of these systems. Related work includes cell migration in two-dimensional channels [12,13], cardiac heterogeneities [14], the effects of obstacles on flame propagation [15], fractal surface heat transfer [16,17], or the large work related to excitable chemical systems. Examples are chemical reaction–diffusion waves in mazes [18] and as clocks [19] or spiral wave behavior around light-induced unexcitable cores [20], in fractal heterogeneities [21], their unpinning or termination [22], or drift [23]. Electrochemistry is another field in which wave propagation on microstructured surfaces has been investigated. Examples are the catalytic oxidation of carbon monoxide on platinum surfaces with inert titanium boundaries [24] or on Pt–Ti, Pt–Rh, and Pt–Pd composite catalysts [25], the catalytic reduction of NO with CO on Pt(100) surfaces with inert Ti/TiO<sub>2</sub> and reactive Rh boundaries [26], or the catalytic methanol oxidation on macroscopic VO<sub>x</sub> islands on Rh(110) surfaces [27].

Section 2 gives a short description of our reaction–diffusion model. Sections 3 and 4 evaluate the propagation dynamics of wavefronts interacting with polygons and Archimedean spirals, respectively. We explore the difference between

<sup>\*</sup> Correspondence to: The College of Wooster, Department of Physics, 1189 Beall Avenue, Wooster, OH 44691, USA. E-mail addresses: nmanz@wooster.edu (N. Manz), jlindner@wooster.edu (J.F. Lindner).

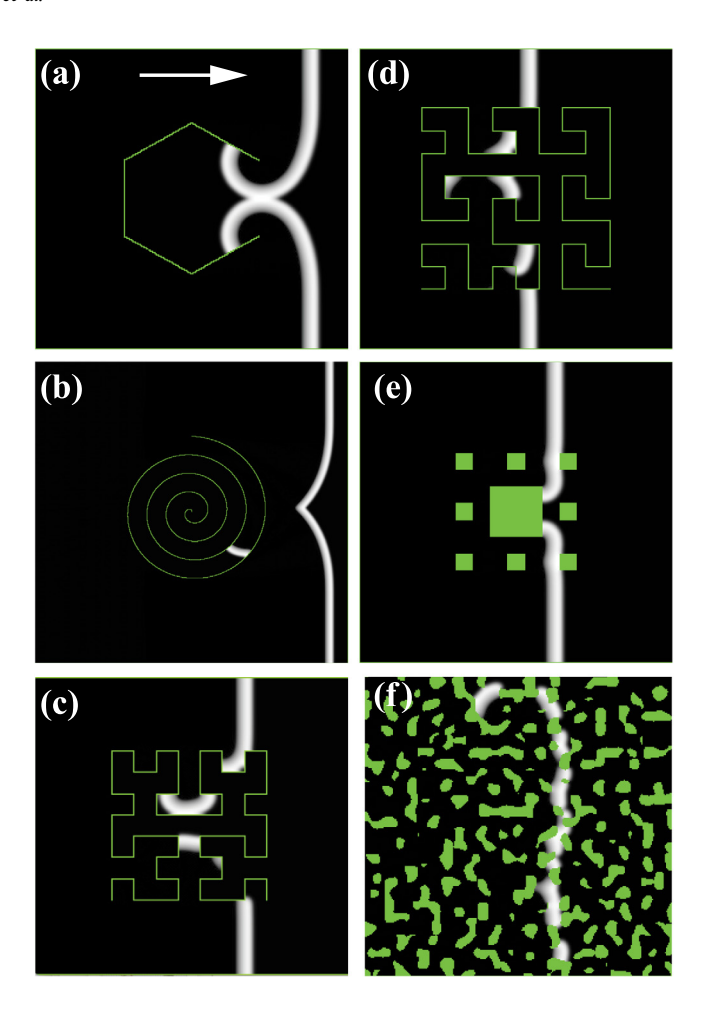


**Fig. 1.** Obstacles. Simulation snapshots of reaction–diffusion wavefronts (gray) encountering various obstacles (green). Waves begin along the left boundary and generally move rightward (white arrow). Brightness of the wavefront is proportional to the activator concentration u[x, y, t]. (a) Concave polygons. (b) Archimedean spirals. (c) Hilbert curves. (d) Peano curves. (e) Sierpinski carpets. (f) Perlin-noise-generated randomness.

concave and convex polygons and show that Archimedean spirals can trap wavefronts for long times. Section 5 studies fractal-like obstacles such as Hilbert and Peano curves, which can multiply wavefronts and also trap wavefront segments for long times. In this section, we also investigate the effect of obstacles in the shape of inverse Sierpinski carpets. Section 6 investigates randomly shaped and placed Perlin-noise-generated obstacles. Finally, Section 7 explores soft obstacles whose propagation condition change gradually, either by varying the diffusivity or the system's reactivity (i.e., light sensitivity). We use such gradients to implement diffusive diodes and clocks: obstacle-reaction-diffusion systems with "heart beats". Section 8 summarizes lessons learned.

#### 2. Reaction-diffusion model

Our computer simulations are based on the Tyson–Fife two-variable reduction [28] of the Oregonator model [29] that describes the Belousov–Zhabotinsky reaction [5,6], a famous family of oscillating chemical reactions. With activator u[x, y, t] and inhibitor v[x, y, t] concentrations changing in space x, y and time t, we add to our previous simulation [11] a light-sensitivity parameter  $\phi$  [30,31] to obtain the reaction equations

$$R_u[u,v] = \frac{1}{\epsilon} \left( u - u^2 + (fv + \phi) \frac{q - u}{q + u} \right),\tag{1a}$$

$$R_{v}[u,v] = u - v,\tag{1b}$$

**Table 1** Polygon simulation parameters.

Symbol	Name	Value
q	Rate constant	0.002
$\epsilon$	Rate constant	0.01
f	Stoichiometric factor	4.0
u <sub>e</sub>	Excited state	0.8
$v_{s}$	Steady state	0.003333
$D_u$	Activator diffusion	1.0
$D_v$	Inhibitor diffusion	0.6
dt	Time step	0.003125
ds	Space step	0.125
N <sub>x</sub>	Channel width	512
$N_y$	Channel height	256

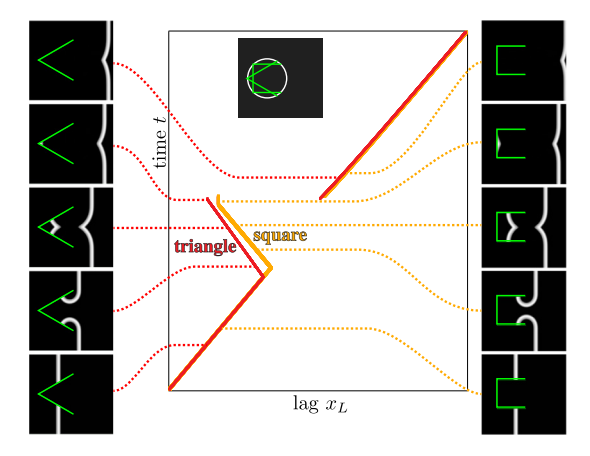


**Fig. 2.** Time *t* versus lag *x*<sub>L</sub> for a wavefront interacting with an open triangle (red) and open square (orange). Sidebars (left and right) are simulation snapshots of the corresponding wavefront propagation, with time increasing upward. Top insert shows the triangle and square inscribed in a common circle.

which represent fast and slow chemical reactions with rate and stoichiometric parameters  $\epsilon \ll 1$ ,  $q \ll 1$ , and  $f \sim 1$ . The diffusion equations for the activator and the inhibitor are

$$\partial_t u = \vec{\nabla} \cdot \left( D_u \vec{\nabla} u \right),$$
 (2a)

$$\partial_t v = \vec{\nabla} \cdot \left( D_v \vec{\nabla} v \right), \tag{2b}$$

with the diffusion coefficients  $D_u[x, y]$  and  $D_v[x, y]$  possibly varying in space, but typically  $D_u \gtrsim D_v \sim 1$ . Then the coupled partial differential reaction-diffusion equations

$$\partial_t u = R_u + \vec{\nabla} \cdot \left( D_u \vec{\nabla} u \right), \tag{3a}$$

$$\partial_t v = R_v + \vec{\nabla} \cdot (D_v \vec{\nabla} v) \,, \tag{3b}$$

represent the Tyson-Fife model for  $\phi=0$ . To realize impermeable obstacles and channel walls, we enforce Neumann noflux boundary conditions [11]. We start our wavefronts with a narrow excitation strip on the left consisting of nonzero activator and zero inhibitor, with zero activator and nonzero inhibitor everywhere else. We numerically integrate Eq. (3) using Forward-Time Central-Space (FTCS) finite differencing with the  $\Delta t \ll \Delta s^2$  stability condition. We use  $\Delta t = \Delta s^2/5$ for all hard obstacle simulations and more stringent conditions for soft obstacles. Our custom multi-threaded Objective-C simulations run on desktop computers.

For open (concave) and closed (convex) polygons, spirals, fractals (Hilbert curve, Peano curve, and Sierpinski carpet), and randomness, the diffusion coefficients  $D_u$  and  $D_v$  are constant and illumination is set to  $\phi = 0$ . To generate time-periodic wavefronts, as discussed in Section 7, the diffusion coefficients or the light sensitivity parameter vary spatially, so wavefronts can propagate one way through a channel but not the other way.

# 3. Polygonal obstacles

We begin with the interaction of reaction-diffusion wavefronts with hard obstacles consisting of convex polygons or concave polygons that resemble regular polygons with a missing side; the former we call **closed**, and the latter we call

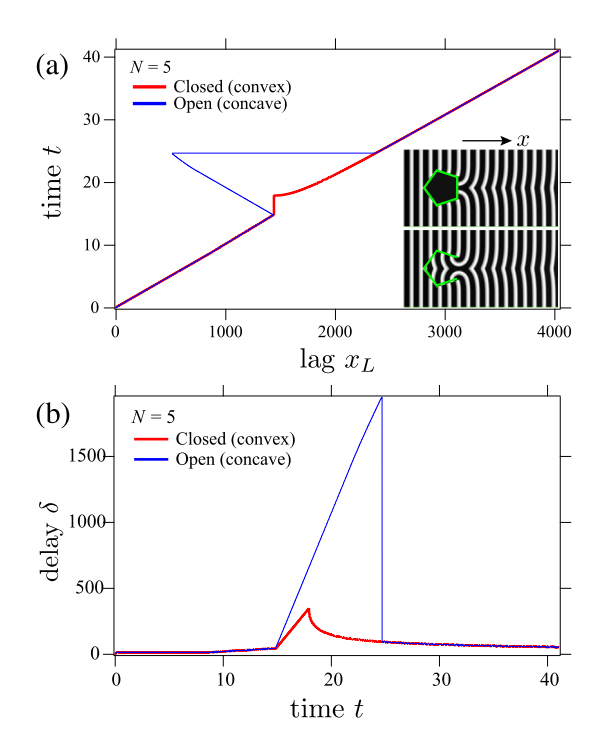


**Fig. 3.** Pentagons. (a) Time t versus lag  $x_L$  for closed (red) and open (blue) pentagons. Open pentagon causes longer delay, due to the motion of the front in the opposite direction, but long time behavior is the same. Inset shows strobed wavefront evolution; the bottom pentagon opens on the down-stream side, and initial propagation direction is rightward. (b) Delay  $\delta$  versus time t. Long time behavior of the open pentagon is the same as that of the closed pentagon.

**open.** Polygons range from triangles (N = 3) to near-circle hectogons (N = 100). The Fig. 1(a) simulation snapshot shows a wavefront interacting with an open hexagon. Table 1 lists the parameters used to numerically solve Eq. (3).

As the wavefront propagates downstream (left-to-right) around the obstacle, we track its leftmost and rightmost points  $x_L$  and  $x_R$ . We call the leftmost point of the wavefront the **lag**  $x_L$  and the difference between the rightmost and leftmost points the **delay**  $\delta = x_R - x_L$ . The red and orange curves of Fig. 2 show time t versus lag  $x_L$  for a wavefront incident on an open triangle and an open square. The kinks in the straight lines are the obstacles' signatures.

We choose a pentagon with N=5 to illustrate the general behavior of wavefronts interacting with concave and convex obstacles. Fig. 3(a) plots the lags and Fig. 3(b) plots the corresponding delays. The latter nicely connects with earlier work [11]. The Fig. 3(a) insets are strobed images of the wavefront interacting with an closed pentagon (top) and an open pentagon (bottom).

A closed pentagon breaks the wavefront into two sections that propagate above and below it. They approach each other along the downstream (vertical) side, generating the vertical jump in the Fig. 3(a) red line, and merge to leave a cusp that shrinks as it flows downstream. An open pentagon also breaks the wavefront into two sections, but these recombine to form an outside downstream wavefront and an inside upstream wavefront. The latter annihilates on the inside of the pentagon, generating the horizontal jump in the Fig. 3(a) blue line.

This effect is largest if the opening of the pentagon is downstream because the initial wavefront sections take longer to enter the inside, and this observation generalizes for all polygonal obstacles. Thus, the open pentagon causes the longer wavefront delay  $\delta$ , as shown in Fig. 3(b). But the downstream wavefront merges and heals with the same power-law dependence [11] as the wavefronts of the closed pentagon.

We systematically increase the number of polygon sides N from 3 to 10 (triangles to decagons) and use 100 (hectogons) to approach the circle limit to investigate the effect of N on the wavefront disruption and recovery. N points equally spaced on an imaginary circle define the polygons with a vertical side downstream, as shown for a triangle and square in Fig. 2. The center of all polygons is fixed in all simulations, which results in the different x-values of the leftmost and rightmost point of the polygons.

In general, the disruption starts later for more-sided polygons, as shown in Fig. 4. The actual disruptions, the vertical jumps in the Fig. 4(a) lag plots, decreases with increasing N due to the vertically shorter downstream side. The sharp transition changes to a curved transition when approaching the circle limit.

While Fig. 4(a) plots the lags for closed N-sided polygons, Fig. 4(b) plots the lags for open N-sided obstacles. The general shape is identical to the example for N=5 in Fig. 3(a) with a leftward moving lag as the wavefront moves upstream inside the polygon. Noteworthy is the much smaller effect of closed N-sided polygons, as can be seen in the limited range on the x and the y axes.

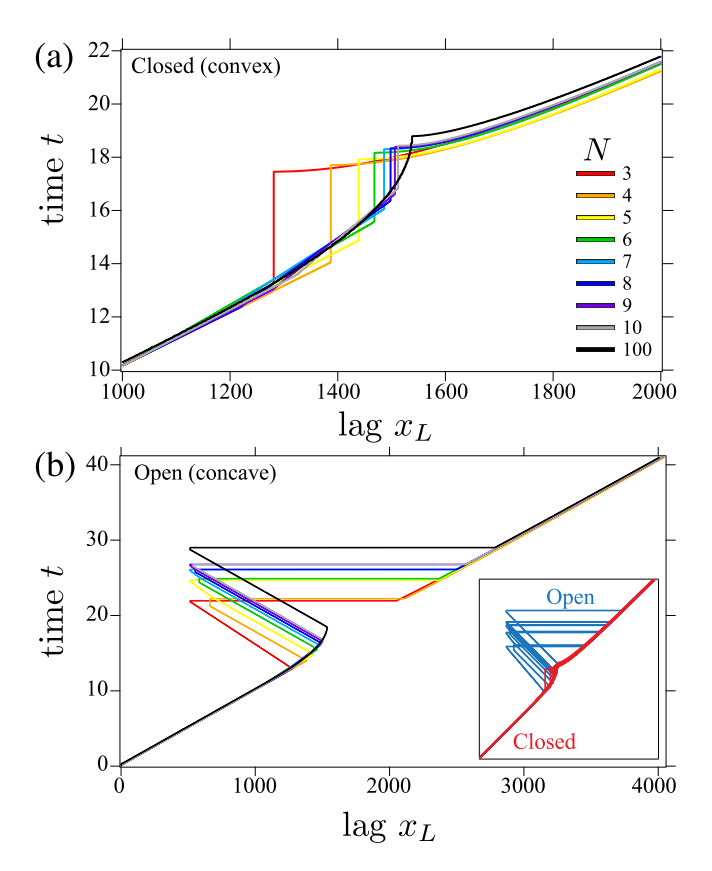


**Fig. 4.** Polygons. (a) Time t versus lag  $x_L$  for closed N-sided polygons. The more sides, the longer delay it causes, but the long time behavior is the same. Jumps occur when the wavefront leaves the right downstream side of the polygon. For the nearly-circular hectogon, the curve reflects the limiting circle. (b) Time t versus lag  $x_L$  for open N-sided polygons. Delays increase with number of sides. The  $x_L$  reversals occur when part of the wavefront enters the polygon and travels backwards. For nearly-circular hectogon, the time-space plot curves before the reversals rather than zigzags.

Polygons with odd numbered sides have the same maximal upstream motion of the front inside the obstacle, reaching the identical smallest  $x_L$  value (the leftmost edge). Even sided polygons have various positions of their upstream and downstream sides. This results in a delayed starting point of the deviation from the initial linear lag behavior and a short time when the lag is constant. Fig. 2 presents a detailed explanation of this feature. After wavefronts interact with open or closed objects, they continue to heal as a power-law function of time.

#### 4. Spiral obstacles

We next present the interaction of reaction–diffusion wavefronts with obstacles consisting of Archimedean spirals whose radius r varies with polar angle  $\theta$  by

$$r = a\frac{\theta - \theta_0}{2\pi} = k(\theta - \theta_0), \qquad (4)$$

where  $\theta_0$  is the orientation of the spiral, a is the radial separation between adjacent spiral arms, and  $k=a/2\pi$  is the "looseness" of the spiral obstacle. The Fig. 1(b) snapshot shows a wavefront encountering a k=5 spiral. As the wave reaches the opening, part of it is trapped and spirals inward until it self-annihilates at the center, which can be long after the rest of the wavefront has moved on and largely healed or even left the simulation space.

We simulate spirals from k = 1 (tightest) to k = 10 (loosest), as summarized by Fig. 5(a). We keep the spiral opening at the top, so the wavefronts always enter in the same way. The spiral geometry generates sinusoidal structure in the t versus  $x_L$  lag plots. The smaller k, the tighter the spiral, and the longer the delay due to the larger number of rotations. In each case, the recovered wavefront exits the simulation space downstream before the trapped wave section reaches the spiral's center, generating the horizontal line at the tip of the oscillatory lag  $x_L$ .

The Fig. 5(a) left inset enlarges the bottom-left lag oscillations. This is the leftmost section of the spiral. With increasing looseness, the turning point is reached earlier because the width of the channel increases and, therefore, the horizontal distance to the spiral's outer radius increases.

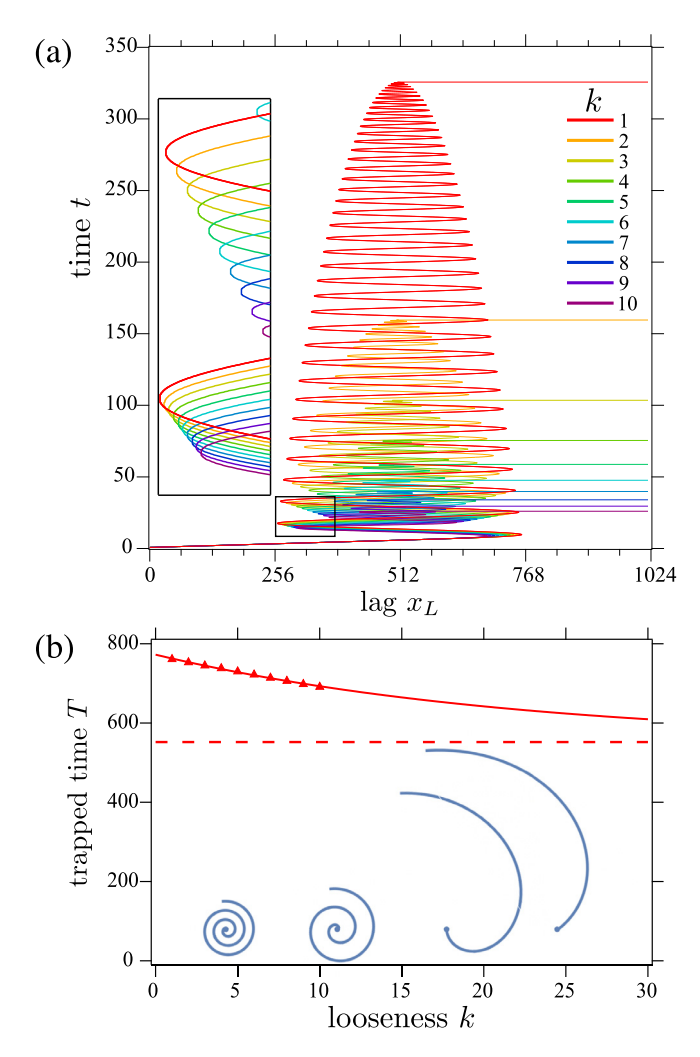


**Fig. 5.** Spirals. (a) Time t versus lag  $x_L$  for spirals from tight (red) to loose (pink) depending on the looseness k. The smaller k, the tighter the spiral, and the larger k, the looser the spiral. Inset magnifies the bottom-left sinusoidal structure of the time-space plot. (b) Trapped time T versus spiral looseness k. Blue insets suggest actual spiral obstacles. As  $k \to \infty$ , the spiral becomes a straight line segment, which eliminates trapping and minimizes delay.

Quantitatively, the trapped time T versus looseness k decreases to a fixed value, which is defined by the x-value of the center of the spirals, as shown in Fig. 5(b). As  $k \to \infty$ , the spiral straightens to a vertical line segment that eliminates trapping and minimizes delay. The dashed line indicates this asymptote.

#### 5. Fractal obstacles

As Mandelbrot famously observed, "Clouds are not spheres, mountains are not cones, coastlines are not circles" [32]. Consequently, we next examine the interaction of wavefronts with obstacles that are (approximately) fractal.

Target fractals include the Hilbert curve [33], the Peano curve [34], and the Sierpinski carpet [35]. The Hilbert and Peano curves are space-filling curves with Hausdorff dimension d=2, but they have different symmetries. The Sierpinski carpet, which is a generalization of the Cantor set [36], is not space filling and has Hausdorff dimension  $d \approx 1.8928$ .

# 5.1. Hilbert curves

The Fig. 1(c) snapshot shows a wavefront encountering an order  $\mathcal{O}=2$  Hilbert curve obstacle. The Hilbert curves are approximate fractals for finite  $\mathcal{O}$  and ideal fractals for  $\mathcal{O}\to\infty$ . We define the Hilbert curve as the limit of the ordered sequence

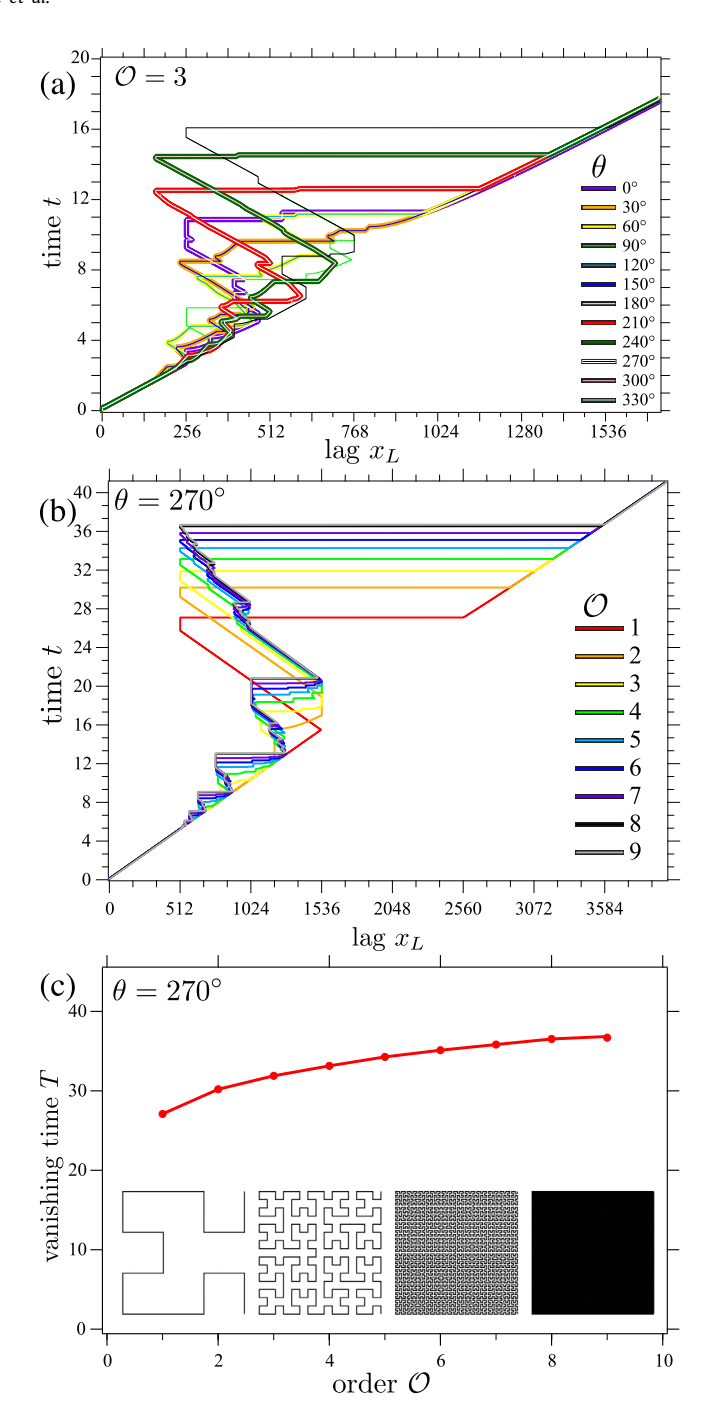


**Fig. 6.** Hilbert. (a) Time t versus lag  $x_L$  for third-order  $\mathcal{O}=3$  Hilbert curve obstacles rotating clockwise in increments of  $\Delta\theta=30^\circ$ . The 10 angles other than  $90^\circ$  and  $270^\circ$  are overlapping pairs, due to symmetry. If the angles are complementary, the symmetrical Hilbert curves are inverted, and the wavefronts are equivalent. (b) Time t versus lag  $x_L$  for Hilbert curve obstacles at angle  $\theta=270^\circ$  for 9 different orders  $\mathcal{O}$ . The higher orders delay the leftmost wavefront point the most. Horizontal lines indicate times when the wavefronts inside the Hilbert curves vanish. Differences between vanishing times decrease as the orders increase. (c) Vanishing time T versus order  $\mathcal{O}$  for the Hilbert curve obstacles at angle  $\theta=270^\circ$ . Vanishing time is when the last internally trapped wavefront segment annihilates. Bottom sketches illustrate orders  $\mathcal{O}=2,4,6$  and 8 Hilbert curves.

and use a computer simulation to generate obstacles with any integer order  $1 \le \mathcal{O} \le 9$  and rotate the curve through any real angle  $0 \le \theta \le 360^\circ$ . Wavefronts interacting with a Hilbert curve breaks into many parts, both wrapping around and interpenetrating it, with many small wave segments simultaneously moving within its maze-like interior for long times.

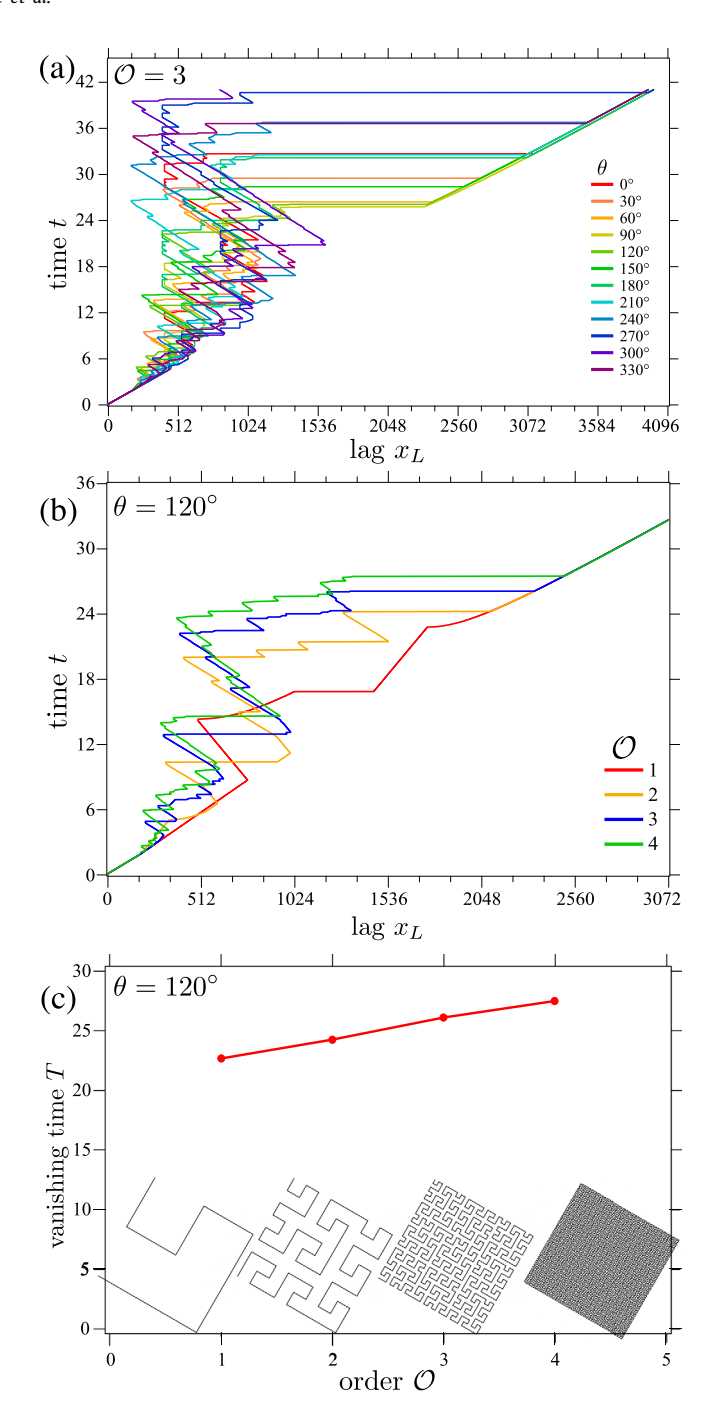


**Fig. 7.** Peano. (a) Time t versus lag  $x_L$  for third-order  $\mathcal{O}=3$  Peano curve obstacles rotating clockwise in increments of  $\Delta\theta=30^\circ$ . The curves are irregular, with none overlapping, because the Peano curve are asymmetrical. But the long time behavior is the same. (b) Time t versus lag  $x_L$  for Peano curve obstacles at angle  $\theta=120^\circ$  for 4 different orders  $\mathcal{O}$ . At higher orders, the wavefront needs longer time to reach the same leftmost point, which means that the wave is trapped longer inside the Peano curve. But again the long time behavior is the same. (c) Vanishing time T versus order  $\mathcal{O}$  for the Peano curve obstacles at angle  $\theta=120^\circ$ . Vanishing time is when the last internally trapped wavefront segment annihilates. Bottom sketches illustrate orders  $\mathcal{O}=1,2,3$  and 4 Peano curves.

Fig. 6(a) is a time t versus lag  $x_L$  plot for a third generation  $\mathcal{O}=3$  Hilbert curve rotating clockwise in increments of  $\Delta\theta=30^\circ$ . The 10 angles other than  $90^\circ$  and  $270^\circ$  are overlapping pairs. If the angles are complementary, the bilaterally symmetric Hilbert curves are inverted, and the wavefronts are equivalent.

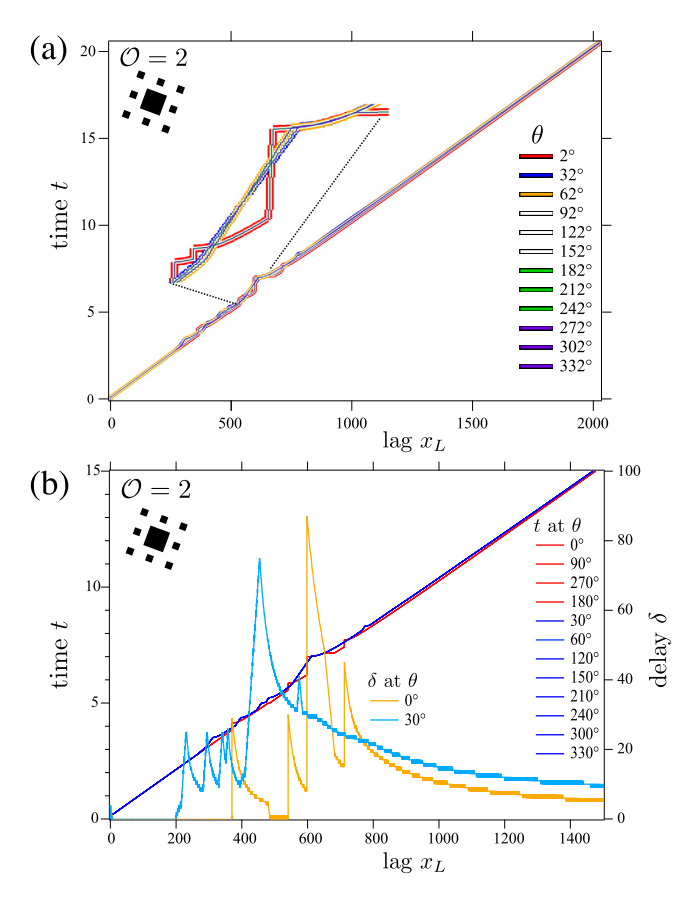


**Fig. 8.** Sierpinski. (a) Time t versus lag  $x_L$  for second order  $\mathcal{O}=2$  Sierpinski carpet obstacles rotating clockwise in increments of  $\Delta\theta=30^\circ$  (red and blue). Only two kinds of behaviors exist, and a delay-space plot accentuates the difference (gold and cyan). (b) Time t versus lag  $x_L$  for the Sierpinski carpet obstacles rotating through more generic angles from  $\theta=2^\circ$  to  $\theta=332^\circ$  in increments of  $\Delta\theta=30^\circ$ . Inset magnifies a portion of the plot to show three distinct behaviors from angles separated by  $30^\circ$ ,  $60^\circ$ , and  $90^\circ$ .

Fig. 6(b) is a t versus lag  $x_L$  plot for a Hilbert curve at angle  $\theta = 270^\circ$  for the first 9 orders  $\mathcal{O}$ . This angle has the most effect because the "opening of the fractal" points downstream (rightward). The higher orders delay the vanishing of the leftmost wavefront inside the Hilbert curves the most. Fig. 6(c) plots the vanishing times T versus the order  $\mathcal{O}$ . As the Hilbert order  $\mathcal{O} \to \infty$ , we expect the vanishing time  $T \to \infty$ .

#### 5.2. Peano curves

The Fig. 1(d) snapshot shows a wavefront encountering a order  $\mathcal{O}=2$  Peano curve obstacle. Like the Hilbert curves, the Peano curves are approximate fractals for finite  $\mathcal{O}$  and ideal fractals for  $\mathcal{O}\to\infty$ . We define the Peano curve as the limit of the ordered sequence

and use a computer simulation to generate obstacles with any integer order  $1 \le \mathcal{O} \le 4$  and rotate the curve through any real angle  $0 \le \theta \le 360^\circ$ . Wavefronts interacting with a Peano curves break into many parts, engulfing and invading it, with multiple small segments exploring its asymmetric maze-like interior for long times.

The plots of Figs. 7(a) and 7(b) summarize the phenomenology, which is similar to that of the Hilbert curve obstacles, but without the Hilbert curves' bilateral symmetry, the dynamics is less ordered and more irregular. Each angle creates its own graph without any overlaying lines, as for the Hilbert curve graph in Fig. 6(a). The wavefronts are trapped much longer inside the higher order curves, as witnessed by the different time axes for  $\mathcal{O}=3$  Hilbert and Peano curves in Figs. 6(a) and 7(a).

Unsurprisingly, the vanishing times for Peano curves also increase as the orders increase. Fig. 7(c) plots vanishing time T versus order  $\mathcal{O}$  for the Peano curve at angle  $\theta=120^\circ$ . Vanishing time is when the last internal wavefront segment

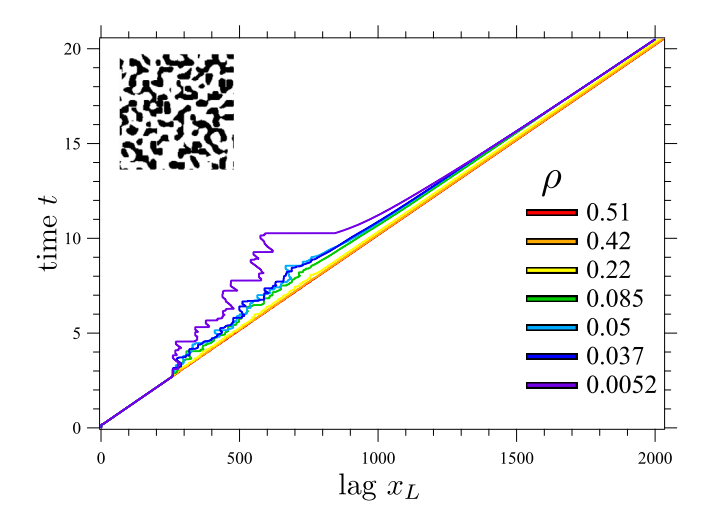


**Fig. 9.** Time t versus lag  $x_L$  for Perlin-noise-generated random obstacles of different densities  $\rho$ . Higher densities cause longer delays, until propagation stops completely at a percolation threshold. The inset in the top left corner has a density of  $\rho \sim 0.05$ .

annihilates, the resonant time of the wavefront segments trapped inside the Peano curve. As the Peano order  $\mathcal{O} \to \infty$ , we expect the vanishing time  $T \to \infty$  so the internal wavefront is forever trapped inside the infinitely long ideal Peano curve. The insets illustrate the orders  $\mathcal{O} = 1, 2, 3$  and 4 Peano curves.

### 5.3. Sierpinski carpets

The Fig. 1(e) snapshot shows a wavefront encountering a order  $\mathcal{O}=2$  Sierpinski carpet. Unlike the Hilbert and Peano fractals, the Sierpinski carpet is not space-filling. We define the (inverse) Sierpinski carpet as the limit

and simulate wavefronts interacting with various orders of the carpet rotated through multiple angles. Each component square in the carpet bends the wavefront, with the large central square bending most. The carpet's open structure causes less wavefront disruption than the previous fractals, and its greater 4-fold symmetry organizes the results.

Fig. 8(a) is a time t versus lag  $x_L$  plot for the second order  $\mathcal{O}=2$  Sierpinski carpet rotating clockwise in increments of  $\Delta\theta=30^\circ$  (red and blue lines). Only two kinds of behaviors exist due to the 4-fold symmetry: the red line for arrangements perpendicular to the propagation direction and the blue line for all other arrangements at the specified rotation angles. The delay  $\delta$  versus lag  $x_L$  plot accentuates the difference between the perpendicular case (gold) and the angled case (cyan).

More generically, Fig. 8(b) presents the same time versus lag plot for an  $\mathcal{O}=2$  Sierpinski carpet rotating clockwise in increments of  $\Delta\theta=30^\circ$  as in Fig. 8(a) but now through angles from  $\theta=2^\circ$  to  $\theta=332^\circ$ . Starting at an angle different than zero, such as  $\theta=2^\circ$ , is necessary to obtain any clear varying behavior, as seen in the enlarged section. The inset magnifies a portion of the plot to show three distinct behaviors corresponding to angles separated by 30°, 60°, and 90°.

#### 6. Random obstacles

All the previous obstacles, even the fractals, were regular. But nature often appears irregular [37] and complex labyrinths and patterned media are of great interest [18,38]. To simulate an irregular reaction–diffusion system, we used Perlin noise [39] to generate random obstacles with adjustable average density  $0 \le \rho \le 1$ , where  $\rho = 0$  is an empty channel and  $\rho = 1$  is a full channel. The Perlin algorithm, which won a 1997 Academy Award, uses random gradients to produce natural textures for computer-generated special effects in motion pictures, such as mountains and water waves. Our implementation of Perlin noise fills a fraction of the channel with solid obstacles, and the Fig. 1(f) snapshot shows a wavefront navigating a Perlin-noise generated obstacle field with  $\rho \sim 0.05$ .

We find a percolation-like transition at a density of  $\rho \sim 0.5$  above which propagation does not occur. The time t versus lag  $x_L$  plot in Fig. 9 summarizes the low-density phenomenology. Very low densities only slightly delay the wavefronts, but higher densities cause greater delays, with the wavefronts breaking apart, reversing, and reconnecting until they are stopped altogether at the percolation threshold.

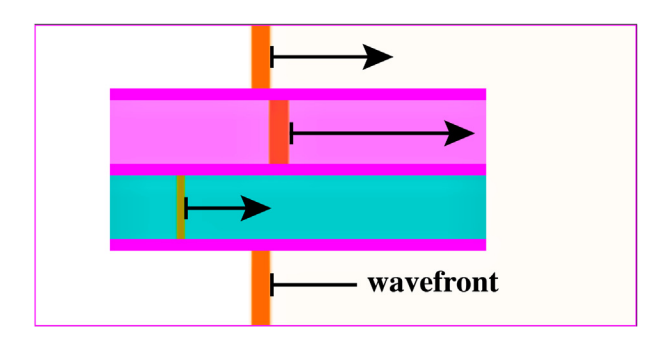


**Fig. 10.** Simulation snapshot of a wavefront (vertical orange line segments) traveling left-to-right in channels with different diffusivities. The top channel has larger diffusivity  $1 < D_u$ , and the bottom channel has smaller diffusivity  $0 < D_u < 1$ . The wavefront in the top channel propagates faster than the wavefront in the bottom channel and outraces the latter.

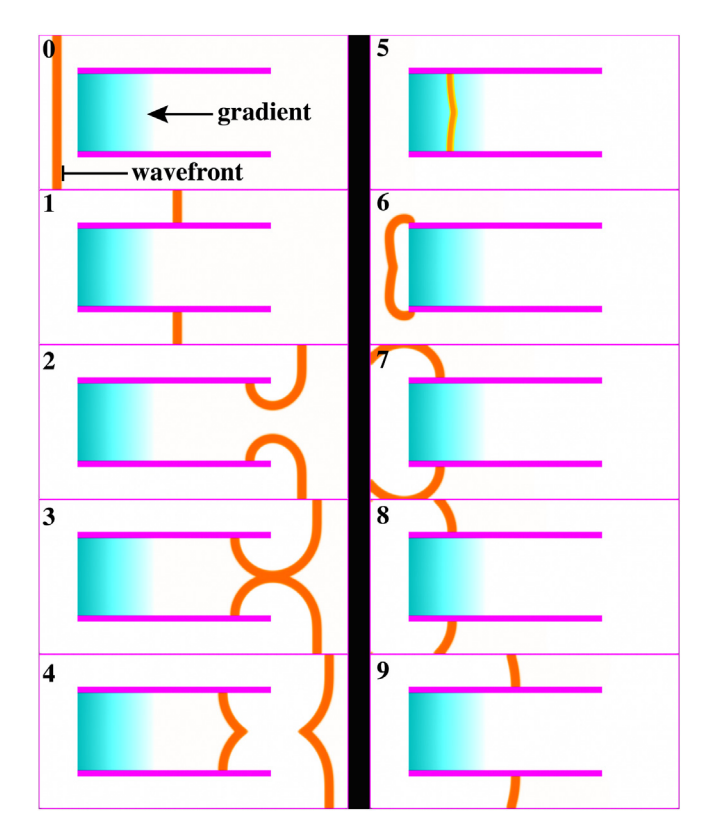


**Fig. 11.** Selected simulation frames at variable time intervals  $\Delta t$  summarize the behavior of a clock or repeater. Soft obstacle with variable diffusivity  $0.25 \le D_u \le 1$  (cyan gradient) allows the wavefront to propagate upstream (right-to-left) but not downstream (left-to-right). This pattern repeats indefinitely as long as the medium remains excitable. Other constant simulation parameters:  $D_v = 0.4$  and  $\phi = 0$ .

#### 7. Soft obstacles

Previous models involve hard obstacles [40], which can be characterized as regions of zero diffusivity. We found that such obstacles can delay reaction-diffusion wavefronts and resonate with segments of them for long times, but eventually the segments self-annihilate (except in ideal limits). Here we consider soft obstacles [41] characterized by regions of variable diffusivity that can sustain wavefronts indefinitely. Such 'chemical clocks' were first proposed by Motoike et al. [42] using narrow gaps in excitability that enforced one-way propagation.

As a proof-of-concept, Fig. 10 illustrates a wavefront (orange) traveling left-to-right in channels (magenta) with different diffusivities. At constant inhibitor diffusivity  $D_v$ , we vary the activator diffusivity  $D_u$ . The top channel has larger diffusivity  $1 < D_u$ , the bottom channel has smaller diffusivity  $0 < D_u < 1$ , and the background (white) has intermediate diffusivity  $D_u = 1$ . The wavefront in the top channel propagates faster than the wavefront in the bottom channel (and the wavefront in the background) and the former outraces the latter.

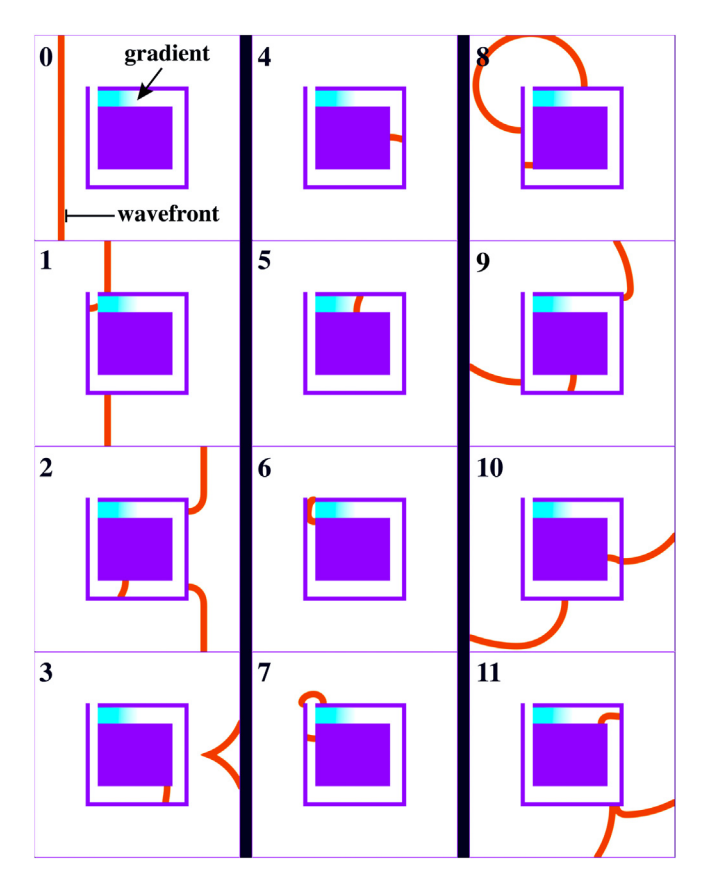


Fig. 12. Soft obstacle with variable diffusivity (cyan gradient) allows wavefronts to circulate counter clockwise but not clockwise inside the square channel, creating a compact clock or repeater.

# 7.1. Variable diffusivity

Next, we form a one-way channel [43] or diffusive diode by plugging a hard channel with a gradient soft obstacle whose diffusivity increases linearly from  $D_u = 0.25$  on the upstream (left) side to the background  $D_u = 1$  on the downstream (right) side, as indicated by the cyan gradient in Fig. 11. The abrupt decrease in diffusivity at the channel opening extinguishes the wavefront's propagation ability. Meanwhile, the wavefront outside the obstacle propagates around it, partly reenters from the downstream side, and propagates upstream while continuously adapting to the gradual decrease in diffusivity. Finally, it leaks out the left side, curls around, and propagates downstream again. The system cycles like a clock, as long as the medium remains excitable [44].

The Fig. 12 simulation sequence shows a compact clock with a square geometry. The soft obstacle with variable diffusivity (cyan gradient) allows wavefronts to circulate counterclockwise but not clockwise inside the square channel, so wavefronts repeatedly leak out the top to initiate a new wavefront for the system. By keeping the soft obstacle parameters constant, the frequency of wave generation can be modulated by changing the path length within the clock.

This frequency modulated clock-like behavior could have been accomplished with a non-excitable gap, as discussed by Motoike and Yoshikawa [45]. They showed that a wavefront propagating normal to a non-excitable gap can excite the medium beyond it from one direction but not the other. But with a diffusion gradient, one can change the wave generation frequency by manipulating the gradient while keeping the channel length of the clock constant. This is a much more flexible approach than a non-excitable gap that has defined limits beyond which the wave penetration becomes impossible.

# 7.2. Light sensitivity

A more practical way to create diffusive diodes is to exploit the light sensitivity of some excitable media [30,31], which we model with the Eq. (1) parameter  $\phi$ . We keep the activator diffusivity  $D_u = 1$  and vary  $\phi$  via changing illumination, effectively creating a soft obstacle.

The Fig. 13 simulation features a one-way channel or diffusive diode (blue gradient) caused by varying the light intensity from dim to bright, corresponding to  $0 < \phi < 0.0344$ . As the wavefront enters the channel, it moves slower

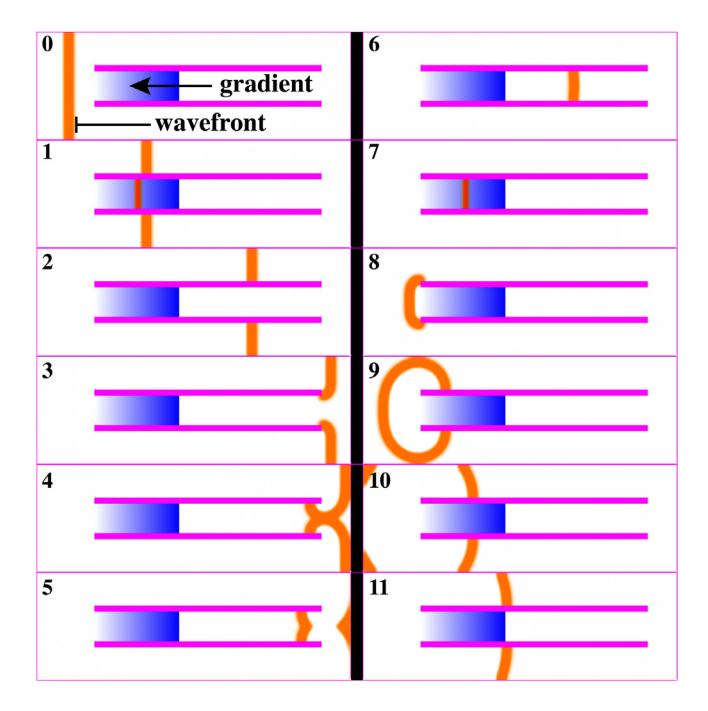


**Fig. 13.** Simulation sequence with variable  $\Delta t$  between the shown frames to capture the system's behavior. The system's diffusivity is constant but the soft obstacle has variable illumination  $0 < \phi < 0.0344$  (blue gradient) and also creates a one-way channel and repeater.

and slower downstream (left-to-right) due to the increasing brightness gradually eroding until it vanishes with nothing leaking out downstream. Meanwhile, the wavefront outside the obstacle propagates around it, partly reenters from the right side, propagates to the left, and leaks out on the left side. Similar to the previous diode, the system repeats like a clock, as long as the medium remains excitable and the light gradient is maintained.

As with the diffusion diode, a similar arrangement as shown in Fig. 12 could create a clock with an easy-to-manipulate frequency range.

### 8. Conclusion

This work extends previous work on the interaction of reaction–diffusion wavefronts with hard convex obstacles [11] to a wide variety of other obstacles. We again observe disruption and recovery of the wavefronts with a healing power-law function of time. Concave polygons do allow wavefronts to enter them and propagate upstream for short times before annihilating.

Spiral obstacles can sustain wavefront motion for long times, limited in practice by the narrowness of the spiral walls and the width of the channel that allow the reaction–diffusion wavefront to propagate. (Wavefronts can propagate within exceedingly thin channels, but they can detach at sharps turns [24] and annihilate at the opposite wall if the channel width is smaller than the core radius plus a critical radius.) Fractal obstacles can support extended motion of many wavefront segments in fascinating patterns, again limited mainly by the narrowness of their maze-like features. Random objects exhibit a percolation threshold, a critical density above which the reaction–diffusion wavefronts will not propagate.

Soft obstacles with a propagation condition gradient can form unidirectional channels (propagation diodes). This can be achieved by varying the diffusivity of the medium (e.g., space-dependent material property of a gel) or because of illumination gradient applied to a light-sensitive system. These gradients can be used to create clocks and repeaters that can sustain wavefront activity indefinitely in, for example, a batch reactor. Such clocks might serve as the "heart beat" for reaction–diffusion computers [46] and provide insight into biological pacemakers. They are vivid and spectacular examples of the possibilities and potential of excitable media. **Animations of our simulations are available online as a supplement to this article.** 

#### **CRediT** authorship contribution statement

Yang F. Yu: Software, Validation, Writing - original draft. Chase A. Fuller: Software, Validation. Margaret K. McGuire: Software, Writing - review & editing. Nathaniel J. Smith: Software. Niklas Manz: Conceptualization, Resources, Writing - original draft, Supervision, Funding acquisition. John F. Lindner: Methodology, Software, Resources, Writing - original draft, Visualization, Funding acquisition.

#### **Declaration of competing interest**

The authors declare that they have no known competing financial interests or personal relationships that could have appeared to influence the work reported in this paper.

#### Acknowledgments

This work was supported by the Sherman Fairchild Foundation, USA, National Science Foundation - Division of Materials Research, USA DMR-1560093 and DMR-1852095, and The College of Wooster, USA.

#### Appendix A. Supplementary data

Supplementary material related to this article can be found online at https://doi.org/10.1016/j.physa.2020.125536.

#### References

- [1] F. Siegert, C.J. Weijer, Digital image processing of optical density wave propagation in and analysis of the effects of caffeine and ammonia, J. Cell Sci. 93 (2) (1989) 325–335.
- [2] N. Suzuki, M. Hirata, S. Kondo, Traveling stripes on the skin of a mutant mouse, Proc. Natl. Acad. Sci. 100 (17) (2003) 9680–9685, http://dx.doi.org/10.1073/pnas.1731184100.
- [3] S. Jakubith, H.H. Rotermund, W. Engel, A. von Oertzen, G. Ertl, Spatiotemporal concentration patterns in a surface reaction: Propagating and standing waves, rotating spirals, and turbulence, Phys. Rev. Lett. 65 (24) (1990) 3013–3016, http://dx.doi.org/10.1103/PhysRevLett.65.3013.
- [4] K. Krischer, Principles of temporal and spatial pattern formation in electrochemical systems, in: B.E. Conway, J.O. Bockris, R.E. White (Eds.), Modern Aspects of Electrochemistry, Number 32, Kluwer Academic / Plenum Publishers, New York, 1999, pp. 1–142.
- [5] B.P. Belousov, Periodically acting reaction and its mechanism, Collect. abstr. radiat. med. 1958 1 (1959) 145-147.
- [6] A.M. Zhabotinsky, Periodic course of oxidation of malonic acid in solution (Investigation of the kinetics of the reaction of Belousov), Biophysics 9 (3) (1964) 329–335.
- [7] V. Koroleva, J. Bureš, Circulation of cortical spreading depression around electrically stimulated areas and epileptic foci in the neocortex of rats, Brain Res. 173 (2) (1979) 209–215, http://dx.doi.org/10.1016/0006-8993(79)90622-X.
- [8] R.A. Gray, A.M. Pertsov, J. Jalife, Spatial and temporal organization during cardiac fibrillation, Nature 392 (6671) (1998) 75–78, http://dx.doi.org/10.1038/32164.
- [9] R.J. Stevens, J.S. Weinert, N.G. Publicover, Visualization of origins and propagation of excitation in canine gastric smooth muscle, Am. J. Physiol. Cell Physiol. 277 (3) (1999) C448–C460, http://dx.doi.org/10.1152/ajpcell.1999.277.3.C448.
- [10] E. Pervolaraki, A.V. Holden, Spatiotemporal patterning of uterine excitation patterns in human labour, Biosystems 112 (2) (2013) 63–72, http://dx.doi.org/10.1016/j.biosystems.2013.03.012.
- [11] N.J. Smith, R. Glaser, V.W.H. Hui, J.F. Lindner, N. Manz, Disruption and recovery of reaction-diffusion wavefronts colliding with obstacles, Physica A 517 (2019) 307–320, http://dx.doi.org/10.1016/j.physa.2018.11.024.
- [12] E. Abbena, S. Salamon, A. Gray, Modern Differential Geometry of Curves and Surfaces with Mathematica, Chapman and Hall/CRC, 2017.
- [13] S.-Z. Lin, D. Bi, B. Li, X.-Q. Feng, Dynamic instability and migration modes of collective cells in channels, J. R. Soc. Interface 16 (156) (2019) 20190258, http://dx.doi.org/10.1098/rsif.2019.0258.
- [14] S. Alonso, M. Bär, Reentry produced by small-scale heterogeneities in a discrete model of cardiac tissue, J. Phys. Conf. Ser. 727 (2016) 012002, http://dx.doi.org/10.1088/1742-6596/727/1/012002.
- [15] D. Park, A. Green, Y. Lee, Y. Chen, Experimental studies on interactions between a freely propagating flame and single obstacles in a rectangular confinement, Combust. Flame 150 (1–2) (2007) 27–39, http://dx.doi.org/10.1016/j.combustflame.2007.04.005.
- [16] M. Frank, M. Papanikolaou, D. Drikakis, K. Salonitis, Heat transfer across a fractal surface, J. Chem. Phys. 151 (13) (2019) 134705, http://dx.doi.org/10.1063/1.5115585.
- [17] A. Adamatzky, On interplay between excitability and geometry, Biosystems 187 (2020) 104034, http://dx.doi.org/10.1016/j.biosystems.2019. 104034.
- [18] O. Steinbock, A. Toth, K. Showalter, Navigating complex labyrinths: optimal paths from chemical waves, Science 267 (5199) (1995) 868–871, http://dx.doi.org/10.1126/science.267.5199.868.
- [19] O. Steinbock, P. Kettunen, Chemical clocks on the basis of rotating waves. measuring irrational numbers from period ratios, Chem. Phys. Lett. 251 (5–6) (1996) 305–308, http://dx.doi.org/10.1016/0009-2614(96)00099-1.
- [20] O. Steinbock, S. Müller, Chemical spiral rotation is controlled by light-induced artificial cores, Physica A 188 (1–3) (1992) 61–67, http://dx.doi.org/10.1016/0378-4371(92)90253-M.
- [21] J. Tang, J.-M. Luo, J. Ma, M. Yi, X.-Q. Yang, Spiral waves in systems with fractal heterogeneity, Physica A 392 (22) (2013) 5764–5771, http://dx.doi.org/10.1016/j.physa.2013.07.043.
- [22] J. Luengviriya, M. Sutthiopad, M. Phantu, P. Porjai, J. Kanchanawarin, S.C. Müller, C. Luengviriya, Influence of excitability on unpinning and termination of spiral waves, Phys. Rev. E 90 (5) (2014) 052919, http://dx.doi.org/10.1103/PhysRevE.90.052919.
- [23] E. Nakouzi, J.F. Totz, Z. Zhang, O. Steinbock, H. Engel, Hysteresis and drift of spiral waves near heterogeneities: from chemical experiments to cardiac simulations, Phys. Rev. E 93 (2) (2016) 022203, http://dx.doi.org/10.1103/PhysRevE.93.022203.
- [24] M.D. Graham, I.G. Kevrekidis, K. Asakura, J. Lauterbach, K. Krischer, H.-H. Rotermund, G. Ertl, Effects of boundaries on pattern formation: catalytic oxidation of CO on platinum, Science 264 (5155) (1994) 80–82, http://dx.doi.org/10.1126/science.264.5155.80.
- [25] M. Pollmann, H. Rotermund, G. Ertl, X. Li, I. Kevrekidis, Formation of two-dimensional concentration pulses on microdesigned composite catalyst surfaces, Phys. Rev. Lett. 86 (26) (2001) 6038–6041, http://dx.doi.org/10.1103/PhysRevLett.86.6038.
- [26] N. Hartmann, Y. Kevrekidis, R. Imbihl, Pattern formation in restricted geometries: the NO+CO reaction on Pt(100), J. Chem. Phys. 112 (15) (2000) 6795–6803, http://dx.doi.org/10.1063/1.481254.
- [27] B. von Boehn, R. Imbihl, Chemical wave patterns and oxide redistribution during methanol oxidation on a V-Oxide Promoted Rh (110) Surface, J. Phys. Chem. C 122 (24) (2018) 12694–12703, http://dx.doi.org/10.1021/acs.jpcc.8b00852.
- [28] J.J. Tyson, P.C. Fife, Target patterns in a realistic model of the Belousov-Zhabotinskii reaction, J. Chem. Phys. 73 (5) (1980) 2224–2237, http://dx.doi.org/10.1063/1.440418.

- [29] R.J. Field, R.M. Noyes, Oscillations in chemical systems. IV. Limit cycle behavior in a model of a real chemical reaction, J. Chem. Phys. 60 (5) (1974) 1877–1884, http://dx.doi.org/10.1063/1.1681288.
- [30] V. Gáspár, G. Bazsa, M.T. Beck, The influence of visible light on the Belousov-Zhabotinskii oscillating reactions applying different catalysts, Z. Phys. Chem. 264 (1) (1983) 43–48.
- [31] L. Kuhnert, A new optical photochemical memory device in a light-sensitive chemical active medium, Nature 319 (6052) (1986) 393–394, http://dx.doi.org/10.1038/319393a0.
- [32] B.B. Mandelbrot, The Fractal Geometry of Nature, second ed., W.H. Freeman, San Francisco, 1982.
- [33] D. Hilbert, Ueber die stetige Abbildung einer Line auf ein Flächenstück (about the continuous mapping of a line onto a planar patch), Math. Ann. 38 (3) (1891) 459–460, http://dx.doi.org/10.1007/BF01199431.
- [34] G. Peano, Sur une courbe, qui remplit toute une aire plane (On a curve, which fills an entire flat area), Math. Ann. 36 (1) (1890) 157–160, http://dx.doi.org/10.1007/BF01199438.
- [35] W.F. Sierpiński, Sur une courbe cantorienne qui contient une image biunivoque et continue de toute courbe donnée (On a Cantorian curve which contains a one-to-one and continuous image of any given curve), C. R. Acad. Sci. 162 (1916) 629–632, https://gallica.bnf.fr/ark: /12148/bpt6k3115n/f631.item#.
- [36] G. Cantor, Ueber unendliche, lineare Punktmannichfaltigkeiten (About infinite, linear point manifolds), Math. Ann. 21 (1) (1883) 51–58, http://dx.doi.org/10.1007/BF01442612.
- [37] K.H.W.J. ten Tusscher, A.V. Panfilov, Wave propagation in excitable media with randomly distributed obstacles, Multiscale Model. Simul. 3 (2) (2005) 265–282, http://dx.doi.org/10.1137/030602654.
- [38] O. Steinbock, P. Kettunen, K. Showalter, Anisotropy and spiral organizing centers in patterned excitable media, Science 269 (5232) (1995) 1857–1860, http://dx.doi.org/10.1126/science.269.5232.1857.
- [39] K. Perlin, An image synthesizer, ACM SIGGRAPH Comput. Graph. 19 (3) (1985) 287-296, http://dx.doi.org/10.1145/325165.325247.
- [40] Z. Rostami, K. Rajagopal, A.J.M. Khalaf, S. Jafari, M. Perc, M. Slavinec, Wavefront-obstacle interactions and the initiation of reentry in excitable media, Physica A 509 (2018) 1162–1173, http://dx.doi.org/10.1016/j.physa.2018.06.062.
- [41] V. Zykov, A. Krekhov, E. Bodenschatz, Fast propagation regions cause self-sustained reentry in excitable media, Proc. Natl. Acad. Sci. 114 (6) (2017) 1281–1286, http://dx.doi.org/10.1073/pnas.1611475114.
- [42] I.N. Motoike, K. Yoshikawa, Y. Iguchi, S. Nakata, Real-time memory on an excitable field, Phys. Rev. E 63 (3) (2001) 036220, http://dx.doi.org/10.1103/PhysRevE.63.036220.
- [43] K. Agladze, R.R. Aliev, T. Yamaguchi, K. Yoshikawa, Chemical Diode, J. Phys. Chem. 100 (33) (1996) 13895–13897, http://dx.doi.org/10.1021/ip9608990.
- [44] A.F. Taylor, G.R. Armstrong, N. Goodchild, S.K. Scott, Propagation of chemical waves across inexcitable gaps, Phys. Chem. Chem. Phys. 5 (18) (2003) 3928, http://dx.doi.org/10.1039/b305863h.
- [45] I. Motoike, K. Yoshikawa, Information operations with an excitable field, Phys. Rev. E 59 (5) (1999) 5354–5360, http://dx.doi.org/10.1103/ PhysRevE.59.5354.
- [46] A. Adamatzky, B. De Lacy Costello, T. Asai, Reaction-Diffusion Computers, Elsevier, Amsterdam: Boston, 2005.